Low Velocity Opposed-Flow Flame Spread in a Transport-Controlled Environment DARTFire

Jeff West, Pete Thomas, Ruian Chao, and Subrata Bhattacharjee
Department of Mechanical Engineering
San Diego State University, San Diego, CA 92182-0191

Lin Tang and Robert A. Altenkirch
Department of Mechanical Engineering and NSF/ERC for Computational Field Simulation
Mississippi State University, Mississippi State, MS 39762

Sandra L. Olson
NASA Lewis Research Center
Cleveland, OH 44135

Introduction

Opposed-flow flame spread over a solid fuel is a fundamental combustion problem with applications to fire safety. The forced or free convection configuration for the situation where the opposing oxidizer flow velocity, $\hat{V}_r$, is large compared to the flame spread rate, $\hat{V}_f$, has been subjected to substantial investigation (see for example Refs. [1-3]). Reasonable agreement exists on the physics of the process for $\hat{V}_r / \hat{V}_f >> 1$. In this limit, the flame propagates by transferring heat by conduction to the unburnt fuel ahead of it to raise the fuel temperature from $\hat{T}_\infty$ to the vaporization temperature $\hat{T}_v$. This produces gas-phase fuel to feed the gas-phase flame with species diffusion taking place in the presence of the relatively strong convective bulk oxidizer flow.

While the physics of the flame spread process for $\hat{V}_r / \hat{V}_f >> 1$ are reasonably clear, such is not the case for $\hat{V}_r / \hat{V}_f$ of unit order. This situation may arise in the absence of any externally supplied forced flow in the reduced-gravity environment of spacecraft where natural convection is suppressed. Consequently, our focus in the DARTFire project is on flame spread at reduced or microgravity in an effort to delineate those aspects of the physics of the problem that must be included in flame spread modeling. Modeling efforts are important to spacecraft fire safety issues because, unlike usual experimentation in Earth-bound laboratories, it is difficult to obtain substantial amounts of experimental data under reduced-gravity conditions that have direct application to space travel.

As $\hat{V}_r$ is made close to $\hat{V}_f$, radiation cannot be ignored [4]. For flames spreading into a low-velocity flow or a quiescent environment that can be obtained in microgravity, we anticipate behavior then that is different from that obtained at the higher velocities where radiation is unimportant and transport is relatively fast.

Objectives

The overall objectives of the DARTFire project are to uncover the underlying physics and increase understanding of the mechanisms that cause flames to propagate over solid fuels against a low velocity of oxidizer flow in a low-gravity environment. Specific objectives are 1) to analyze experimentally observed flame shapes, measured gas-phase field variables, spread rates, radiative characteristics, and solid-phase regression rates for comparison with previously developed model prediction capability that will be continually extended, and 2) to investigate the transition from ignition to either flame propagation or extinction in order to determine the characteristics of those environments that lead to flame evolution. To meet the objectives, a series of sounding rocket experiments has been designed to exercise several of the dimensional,

controllable variables that affect the flame spread process over PMMA in microgravity, i.e, the opposing flow velocity (1-20 cm/s), the external radiant flux directed to the fuel surface (0-2 W/cm^2), and the oxygen concentration of the environment (35- 70%). Because radiative heat transfer is critical to these microgravity flame spread experiments, radiant heating is imposed, and radiant heat loss will be measured. These are the first attempts at such an experimental control and measurement in microgravity. Other firsts associated with the experiment are 1) the control of the low velocity, opposed flow, which is of the same order as diffusive velocities and Stefan flows; 2) state-of-the-art quantitative flame imaging for species-specific emissions (both infrared and ultraviolet) in addition to novel intensified array imaging to obtain a color image of the very dim, low-gravity flames.

UV-Visible Imaging

As part of the DARTFire sounding rocket experiment, an intensified array video camera is used to image the flame. This technique has the advantage of increased sensitivity over film (equivalent film ASA numbers can be as high as 180,000 [5]) and therefore can enable direct visualization of radical species by incorporating appropriate filters. It has the disadvantage, however, of imaging only in black and white due to its operational characteristics. Because a color image is strongly desired, in part for comparison with previous film images, a multispectral intensified array camera was obtained that could image with red, green, and blue additive filters (RGB) as well as narrow-bandpass filters for specific excited species. The RGB filtered images can be combined to obtain a 24-bit color composite image of the flame as part of the post-mission image processing.

The intensified array camera (Xybion ISG 240, 768 x 493 pixel array) includes a filter wheel with 6 filters. The rotation rate of the filter wheel is 300 rpm, providing 5 frames per filter per second. Color filters include a red additive dichroic filter with 80% transmission above 610 nm, a green additive dichroic filter with 80% transmission from 505-575 nm, and a blue additive dichroic filter with 80 % transmission below 480 nm. A neutral density filter with 70% transmission is also used to obtain a total intensity measure. Chemiluminescent emissions are imaged through 20 nm bandwidth OH and CH filters at 310 nm and 430 nm. The camera utilizes peak mode to avoid saturation of the bright flames against the dark background and optimizes exposure time for each filter image independently.

Infrared Imaging

Infrared emissions from the combustion products will also be monitored during the DARTFire experiment. A multispectral PtSi detector camera (Inframetrics, Inc. Model Infra-Cam PtSi FPA (256x256 pixel array)) was modified to include a 6-filter internal wheel. Filters include 1.87 μm (H_2O), 4.3 μm (CO_2), 3.4 μm (MMA vapor), 4.8 μm (CO), and two soot filters at 1.6 and 3.8 μm. The filter wheel rotates 1 rev/s, providing 1 image per filter per second, which is recorded for later image processing. The gain is fixed for all filters, so each image must be balanced to provide a similar brightness.

Ground-Based Experiments

Laboratory and low-gravity tests aboard the NASA Learjet have been performed using the cameras. The UV-visible imaging provides very good color reproduction provided the rate of change in the image is slow relative to the 5 Hz framing rate so that proper overlap of the images can be obtained upon recombination. Fortunately, in low gravity, most of the changes occur over significantly longer times. Images from the free radical chemiluminescence show that the peak intensity zone from both excited CH and OH occurs at the same approximate distance from the fuel surface. Excited OH is more evenly distributed across the visible flame than excited CH, which is more localized, and thus, presumably, gives a better idea of where the highest reaction rate zones occur.

Infrared imaging has provided a first glimpse into the species fields in the experiment. Because the image is generated due to the combined influence of the concentration and temperature, accurate modelling of the gas-phase radiation greatly helps interpretation of the results. Results to date indicate that MMA fuel vapor is indeed localized near the surface. CO appears over a fairly thick region in low gravity whereas it occurs over a

thin region in normal gravity. Water and CO_2 extend into the oxidizer side of the flame, but CO_2 extends farthest. This could be due to condensation of the water vapor as it moves into cooler regions, because stoichiometric water concentrations are at least six times the dew point at ambient temperatures.

Imaging of the gaseous species is more straightforward than soot because stoichiometry dictates to a large degree the concentration ranges of the gaseous species. Soot concentration, however, is a very strong function of experimental conditions (especially gravity) and can span several orders of magnitude, so determining the right filters for the soot requires high quality ground-based testing prior to the sounding rocket flights. DARTFire will be flying the sounding rocket hardware on the DC-9 this spring in order to finalize these filter choices.

DARTFire Modeling

The DARTfire experiment is supported by, and results interpreted in concert with, a comprehensive modeling effort that is both analytical and computational, e.g., [6,7].

Model Sweep: A model sweep is carried out in Fig. 1, where the computed spread rate corresponding to various mathematical models is presented for a particular environmental condition for flame spread over a thick slab of PMMA in a fully developed channel flow configuration, i.e., similar to the DARTFire configuration. On the very left of the abscissa (model #1), the spread rate matches (within 99.9%) with the exact solution of de Ris [1], and on the extreme right (model #14) is the experimental result of Fernandez-Pello et al. [2], with the intermediate points being the computational results with the assumptions in the thermal theory of de Ris, i.e., zero hang distance (#2), approximate velocity boundary condition (#3), Oseen flow (#4), constant gas density (#5), no wall blowing (#6), infinite-rate chemistry (#7), known vaporization temperature (#8), constant transport properties (#9), no gas or surface radiation (#10-#12), no radiation feedback (#13), removed one by one. It is immediately noticeable that the Oseen flow assumption, i.e., the assumption of a slug flow for the opposing flow field, is the crudest of all assumptions at both high and low $\hat{V}_g$.

EST: An Extended Simplified Theory (EST) [6] has been developed that gives a closed form approximate solution for the spread rate and the flame structure corresponding to model # 6. In the simplified formulation, the conservation equations are parabolized, $\hat{V}_g$ is replaced with an equivalent velocity $\hat{V}_{eqv} = \nu_{hyd}\hat{V}_g$ to overcome the drawbacks of the Oseen approximation, and a new boundary condition is introduced for $\phi_2 = \frac{\beta_2}{\beta_4}\left[y_F - \beta_1\left(y_O^* - 1\right)\right]$, the second Schvab-Zeldovich coupling function, such that at the vaporizing surface, $\phi_2 = \nu_{lift}\phi_{2,f} = \nu_{lift}\frac{\beta_1\beta_2}{\beta_4}$ where ν_{lift} and ν_{hyd} are unknown coefficients and $\beta_1..\beta_6$ are known parameters ($\frac{y_{O,\infty}}{s}, \frac{\Delta h_c^o}{c_g T_\infty}, \frac{\Delta h_v^o}{c_g T_\infty}, \frac{T_v}{T_\infty}, \frac{\lambda_s}{\lambda_g}, \frac{\hat{\rho}_s\hat{C}_s}{\hat{\rho}_g\hat{C}_g}$). This results in a modified expression for the spread rate:

$$\beta_{thick,EST} \equiv \beta_6\frac{\hat{V}_{f,EST}}{\hat{V}_g} = \gamma_{hyd}\frac{F'^2}{\beta_5} \quad \text{where,} \quad F' \equiv \frac{T_{f,ad,EST} - \beta_3}{\beta_3 - 1}, \quad T_{f,ad,EST} = 1 + \beta_1\left(\beta_2 - \frac{\gamma_{lift}\beta_4 B}{\ln(1+B)}\right). \tag{1}$$

For $\nu_{hyd} = \nu_{lift} = 1$ the spread rate expression of Eq. (1) reduces to the de Ris formula. $\hat{V}_{eqv}$ should be the velocity at the flame leading edge at a distance $\hat{L}_g = \frac{\hat{\alpha}_g}{\hat{V}_g}$ from the surface [8,9]. Depending on the geometry under consideration, γ_{hyd} for the fully developed channel (FDC) and flat-plate (FP) configuration can be evaluated.

$$\gamma_{hyd,FDC} \sim \left(\frac{\hat{\alpha}_g}{\hat{H}\hat{V}_g}\right)^{\frac{1}{2}} = c_{h,FDC}\left(\frac{\hat{\alpha}_g}{\hat{H}\hat{V}_g}\right)^{\frac{1}{2}}, \quad \gamma_{hyd,FP} \sim \left(\frac{\hat{\alpha}_g}{\hat{x}_d\hat{V}_g \,\mathrm{Pr}}\right)^{\frac{1}{4}} = c_{h,FP}\left(\frac{\hat{\alpha}_g}{\hat{x}_d\hat{V}_g \,\mathrm{Pr}}\right)^{\frac{1}{4}} \tag{2}$$

In order to obtain a functional relationship between γ_{lift} and the parameters of the problem, we note that the flame stand-off distance depends on this coefficient. From the one-dimensional solution, it can be shown [1] that the stand-off distance depends on the parameter $\frac{\ln(1+B)}{\beta_1}$. Therefore, we expect γ_{lift} to be a function of $\frac{\ln(1+B)}{\beta_1}$. The hydrodynamic constants, $c_{h,FDC}$ and $c_{h,FP}$ as well as the functional relationship between γ_{lift} and the blowing paramaters are obtained through a series of numerical case studies, resulting in:

$$\gamma_{lift} = 1 + c_{lift}\frac{\ln(1+B)}{\beta_1}. \text{ where, } c_{lift} = 0.09, \text{ and, } c_{h,FDC} = 2.22,\ c_{h,FP} = 0.57. \tag{3}$$

To test the flame spread expression from the EST thoroughly , computations were carried out for two different flow configurations, different oxygen levels ($y_{O,\infty}$), a wide range of opposing velocity ($\hat{V}_g$), different ambient pressures ($\hat{P}_\infty$), different channel heights ($\hat{h}$), and different plate lengths up to the leading edge ($\hat{x}_d$). To present the results on the same plot, we note that Eq. (1) can be written as:

$$\hat{V}_{f,EST} = \gamma_{hyd}\hat{V}_g\frac{F'^2}{\beta_5\beta_6} = \hat{V}_{eqv}f(\beta_i, c_{lift}) \tag{4}$$

The function $f(\beta_i, c_{lift})$ carries with it all the chemical information, and $\hat{V}_{eqv}$ carries the hydrodynamic effects. A plot of $\hat{V}_{f,comp} / f(\beta_i, c_{lift})$ vs. $\hat{V}_{eqv}$ in Fig. 2 collapses all the computed data onto a single line described by Eq. (4). The spread rate data [2] at different oxygen levels are similarly plotted in Fig. 3. Except for relatively high or low $\hat{V}_g$, where the bounds of the thermal regime are crossed, the data agree well with the prediction of the EST.

The Microgravity Regime:

When the opposing flow velocity is reduced, radiation plays a more important role. This is evident from the model sweep of Fig. 1, where at $\hat{V}_g$=1 cm/s the introduction of radiation (model #10 to model #13) reduces the spread rate by almost 70%.

The Pseudo-Steady Hypothesis: For a forced opposing flow over a flat plate, the spreading flame encounters a progressively stronger flow due to the thinning of the boundary layer. As a result, even after the ignition transients subside, the flame behavior changes with time for all three regimes of flame spread: In the thermal regime, V_f increases as γ_{hyd} increases; in the blow-off extinction regime, V_f decreases as the effective residence time decreases [2,3]; and, in the microgravity regime, V_f increases as the radiative effects decline [7].

In Fig. 4, we explore this unsteadiness by comparing a series of steady-state computations for the spread rate with unsteady computations for an evolving flame spreading over a thick fuel bed against an opposing flow velocity of 1 cm/s. In the steady computations the fuel pyrolysis length and the flow development lengths are altered to match the instantaneous values of the evolving flame. After the ignition transients subside, the spread rate decreases because of an increase in the flame length resulting in a weakening influence of the flame trailing edge on the forward heat conduction. As the boundary layer effect becomes established, V_f starts to increase as expected. It is evident from this figure that the application of a quasi steady-state model is reasonable after the initial ignition transients are over.

Spread Rate Predictions of the DARTfire Matrix: The steady-state model as well as the predictions from the de Ris formula and the EST are tabulated in Table 1 for the DARTFire experimental matrix. Because the flame spread rate is dependent on the location of the flame leading edge, the values tabulated correspond to an instant when the flame is at the leading edge of the sample, i.e., 4 cm from the entrance of the tunnel and 2 cm from the ignition source. Note that the EST predicts a spread rate very close to the computations for high $\hat{V}_g$ while the de Ris formula, unable to capture the hydrodynamic effects, overpredicts the spread rate by almost an order of magnitude. The discrepancy between the EST and numerical model computations grows as $\hat{V}_g$ is reduced and radiation effects become dominant, radiation being absent in the EST. With the external radiative flux imposed, V_f jumps as can be expected, the jump providing an indication of the level of importance of radiation, which can be directly compared to experiment.

Infra-red Images: The radiation code developed that is incorporated in the computational model is capable of producing a spectral view of the flame from any given angle. An example is given in Fig. 5 where the side-view intensity contours in the 4.5 μm band are plotted for comparison with future IR images. Comparisons at different bands are expected to provide valuable insight into the species and temperature fields in the spreading flames.

Ox. Level	$\hat{V}_g$	Radiative Power	Spread Rate, (mm/s)		
	(cm/s)	(W)	de Ris	EST	Steady-state Computations
35%	15	0	3.84	0.32	0.36
	5	0	1.75	0.21	0.17
	1	0	0.43	0.1	0.04
	1	1	-	-	0.29
	1	2	-	-	0.52
50%	1	0	0.64	0.15	0.09

Table 1. Spread rate predicted by different methods for the experimental matrix.

Conclusions

The DARTFire experiment, and the supporting modeling effort, is designed to take advantage of recent developments in imaging and the ability to model radiative effects in flame spreading. Comparison of spread rate behavior as the controllable variables, including the radiative field, are exercised, and spectral images of the flame with model prediction will provide insight into the important physics of low-velocity, opposed-flow flame spread, the importance of radiative and transport effects, and delineate those conditions under which ignition evolves to flame spreading and/or extinction.

Acknowledgments: This work was supported by NASA through Contract NCC3-221.

References

1. de Ris, J. N., Twelfth Symp. (Int) on Comb., The Comb. Inst., Pittsburgh, (1969), pp. 241-252.
2. Fernandez-Pello, A.C., Ray, S.R., and Glassman, I., Eighteenth Symposium (International) on Combustion, The Combustion Institute, Pittsburgh, PA, p. 579, (1981).
3. Altenkirch, R.A., Eichhron, R., and Rizvi A.R, Combust. Sci. and Tech., Vol. 32, pp. 49-66, (1983).
4. Altenkirch, R.A., Olson, S.L., and Bhattacharjee, S., "Science Requirement Document for DARTFire", NASA Lewis Research Center, May 1994.
5. Weiland, K.J. AIAA-92-0240, 30th Aerospace Sciences Meeting & Exhibit, Jan. 6-9, 1992, Reno,.
6. Bhattacharjee, S., West, J., and Dockter, S. "A Simplified Theory for de Ris Flame Spread over Thermally thick and Thin Fuel", Combustion and Flame, Accepted for Publication, 1995.
7. Bhattacharjee, S., and Altenkirch, R.A., Twenty-Third (Int) Symp. on Combustion, pp. 1627-1633, The Combustion Institute, Pittsburgh, (1990).
8. Bejan, A., "Convection Heat Transfer", John Wiley and Sons, Inc., 1982.
9. Williams, F.A. Sixteenth Symp. (Int.) on Comb., The Comb. Inst., Pittsburgh, (1976), pp. 1281-1294.
10. West, J., Bhattacharjee, S., Thomas, P., Ramirez, B., and Altenkirch, R.A. 1994, ASME Summer Conference, Colorado Springs, CO pp.29-36.

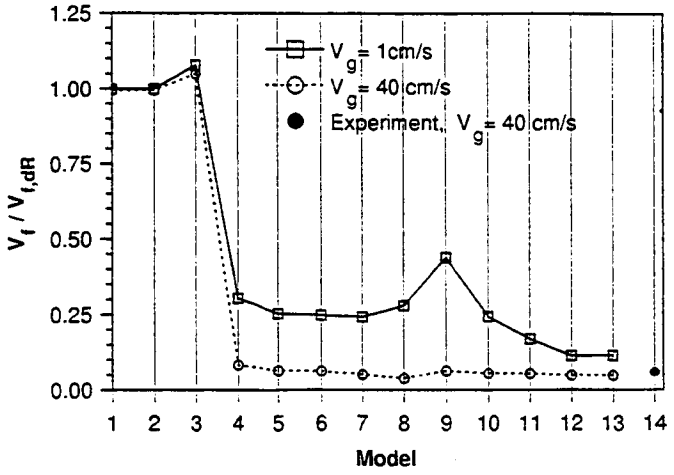

Fig. 1. Computed spread rates for different models. Models on the right are progressively more comprehensive. FDC configuration, $\hat{V}_g$=40 cm/s, 1 cm/s, $y_{O,\infty} = 0.533$, $\hat{P}_\infty$=1.0 atm.

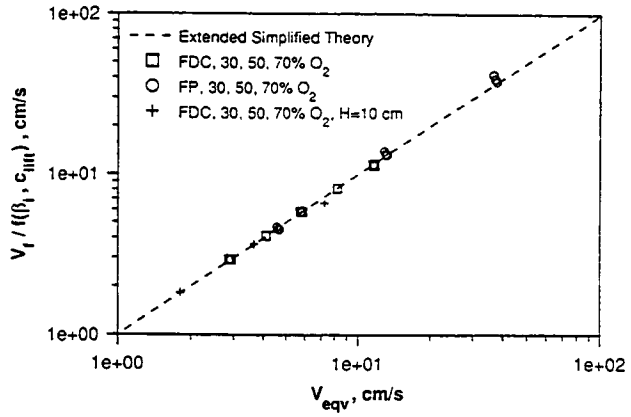

Fig. 2. Computed and EST-predicted spread rates for different flow configurations and ambient conditions.

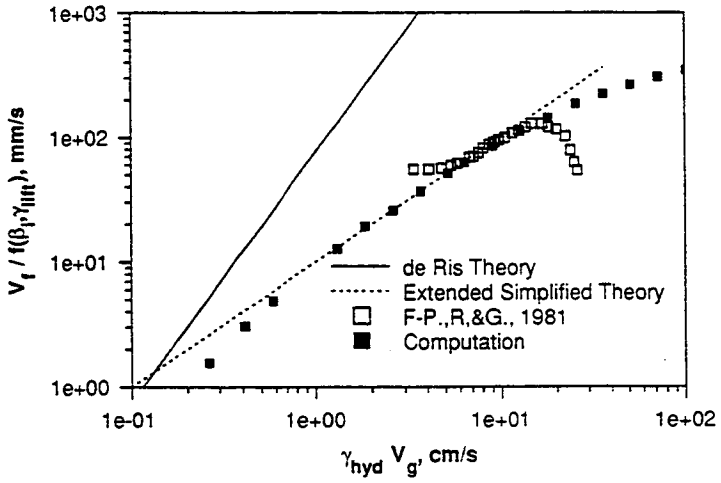

Fig. 3. Experimental data [2] vs. the prediction of EST.

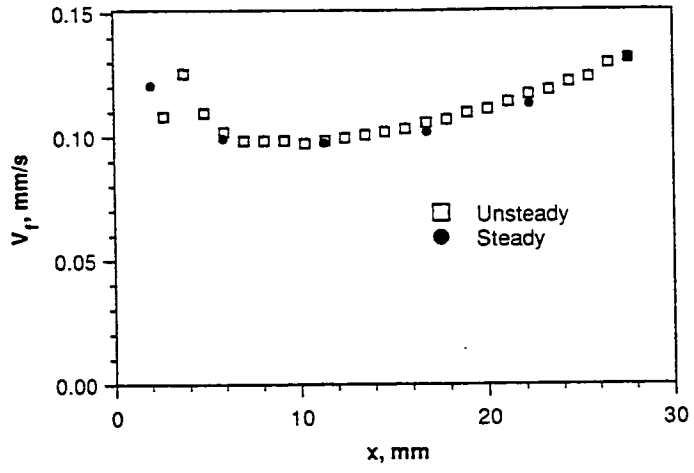

Fig. 4 Spread rate predicted by the steady and the unsteady codes for $\hat{V}_g$ = 1 cm/s, $y_{O,\infty} = 0.533$, $\hat{P}_\infty$=1.0 atm.

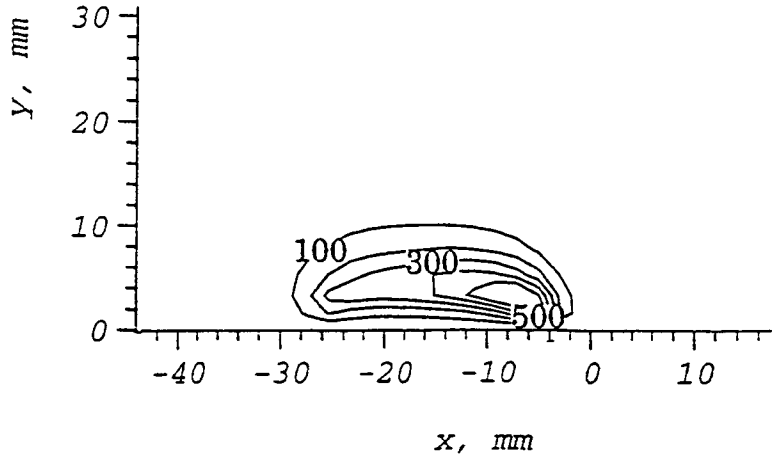

Fig. 5. Intensity contours ($W/m^2.sr$) for the 4.5 micron band for a particular case of the experimental matrix.